JOURNAL OF AIRCRAFT
Vol. 39, No. 4, July–August 2002

Linear and Nonlinear Aeroelastic Analysis of Fighter-Type Wing with Control Surface

Jae-Sung Bae,* Seung-Man Yang,* and In Lee†
Korea Advanced Institute of Science and Technology, Taejon 305-701, Republic of Korea

Linear and nonlinear aeroelastic analyses of a fighter-type wing with a control surface have been performed by using frequency-domain and time-domain analyses. Modes from free vibration analysis and a doublet-hybrid method are used for the computation of subsonic unsteady aerodynamic forces. The fictitious mass modal approach is used to reduce the problem size and the computation time in the linear and nonlinear flutter analyses. For the nonlinear flutter analysis, the control surface hinge is represented by a free-play spring and is linearized by using the describing function method. The linear and nonlinear flutter analyses indicate that the flapping mode of the control surface and the hinge stiffness have significant effects on the flutter characteristics. From the nonlinear flutter analysis, limit-cycle oscillation and chaotic motion are observed in a wide range of air speed below the linear flutter boundary, and a jump of limit-cycle oscillation amplitude is observed.

Nomenclature

$[C]$	=	damping matrix
$\{F\}$	=	external force
$[GK]$	=	generalized stiffness matrix
$[GM]$	=	generalized mass matrix
$[K]$	=	linear stiffness matrix
$[K_n]$	=	stiffness matrix with structural nonlinearity
$[M]$	=	mass matrix
$[\boldsymbol{Q}]$	=	generalized aerodynamic influence coefficient matrix
q	=	dynamic pressure
s	=	free-play angle
U	=	air speed or flight speed
$\{u\}$	=	actual displacement vector
β	=	aerodynamic pole
θ	=	hinge angle of control surface
$[\phi]$	=	modal vector
$[\chi]$	=	transformation matrix
ω	=	natural frequency

Subscripts

b	=	basic model coordinate
f	=	fictitious mass method

Introduction

AEROELASTIC instabilities such as divergence and flutter involve aerodynamic, inertia, and elastic forces of flight vehicles.[1,2] If divergence or flutter occurs in-flight, the aircraft structure may fail or the controllability of the aircraft may decrease. Therefore, it is important to predict the aeroelastic characteristics accurately to prevent aeroelastic instabilities.

Most aeroelastic analyses of flight vehicles have been performed under the assumption of structural linearity. Under this assumption, the characteristics of flutter and divergence can be easily obtained. Structural linearity is based on the assumption that the displacement of the structure is small and that the restoring force is linearly proportional to the displacement. However, the aeroelastic results under the assumption of structural linearity may not agree with the physical phenomena because real structures may have structural nonlinearities. In Ref. 3 structural nonlinearities are discussed. Generally, structural nonlinearities can be subdivided into either concentrated or distributed nonlinearities. Concentrated nonlinearities act locally such as the case of a control surface hinge. Distributed nonlinearities are spread over the entire structure like material nonlinearity, geometric nonlinearity, and buckling. Examples of concentrated nonlinearities are free-play, bilinear, friction, and hysteresis, and these may be caused by a worn or loose hinge of a control surface, or manufacturing tolerances. Distributed nonlinearities have significant effects on the large-amplitude oscillation, whereas concentrated nonlinearities have significant effects on the small-amplitude oscillation. These nonlinearities are usually the function of the amplitude or path of motion. These aeroelastic characteristics are quite different from the linear case. Thus, these structural nonlinearity effects including limit-cycle oscillation must be considered in the aeroelastic analysis.

The aeroelastic response of flight vehicles with a concentrated structural nonlinearity typically include flutter, divergence, limit-cycle oscillation, and chaotic motion. When the linear system becomes unstable, the response is unbounded motion of which the amplitude increases exponentially. However, the nonlinear system has a bounded motion such as limit-cycle oscillation (LCO) or chaotic motion, which may occur below the flutter speed. LCO is a periodic oscillation consisting of a limited number of amplitudes and frequencies, and chaotic motion is a nonperiodic oscillation. The LCO and the chaotic motion do not cause abrupt failure of a structure. However, these motions can cause a structure to be damaged by fatigue and can affect the control systems of flight vehicles. Thus, it is important to understand the nonlinear aeroelastic characteristics of flight vehicles in the design stage.

Nonlinear aeroelastic analyses of a wing with concentrated nonlinearities have been performed by several investigators. Woolston et al.[4] analyzed a relatively simple system including free-play, hysteresis, and cubic nonlinearity and showed that the LCO may occur below the linear flutter boundary. Laurenson and Trn[5] studied flutter of a missile control surface with structural nonlinearities using the describing function method. Lee[6] developed an iterative scheme for multiple nonlinearities using the describing function method and the structural dynamics modification technique. Lee and Tron[7] studied the flutter characteristics of a CF-18 aircraft with structural nonlinearities in the leading-edge flap hinge and the wing-fold hinge using the describing function method. They considered both free-play and bilinear nonlinearities. Yang and Zhao[8] studied the LCO of a typical section model with pitch nonlinearity subject to incompressible flow

Received 2 May 2001; revision received 28 March 2002; accepted for publication 5 April 2002.

*Graduate Research Assistant, Department of Aerospace Engineering.
†Professor, Department of Aerospace Engineering. Senior Member AIAA.

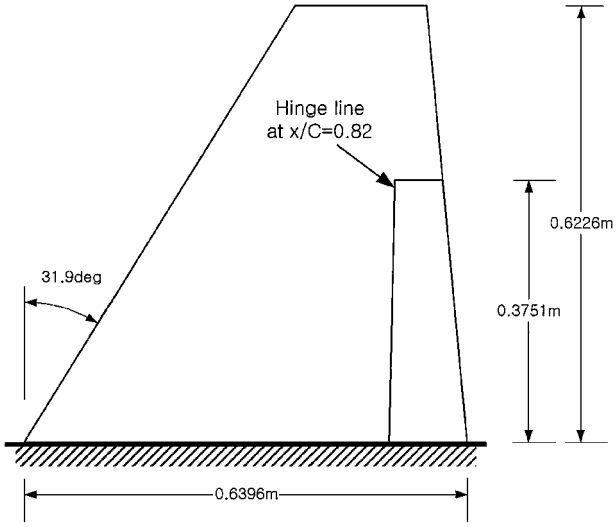

Fig. 1 Configuration of fighter-type wing with control surface.

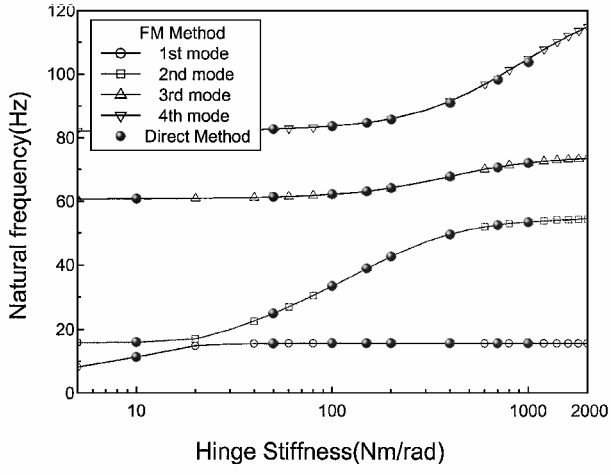

Fig. 2 Natural frequencies vs hinge stiffness.

using the Theodorsen function. Lee and Kim[9] studied the LCO and chaotic motion of a missile control surface with free-play nonlinearity using time-domain analysis. Conner et al.[10] studied the nonlinear behavior of a typical section with control surface free-play both numerically and experimentally.

The purpose of the present study is to analyze the nonlinear aeroelastic characteristics of a fighter-type wing with a structural nonlinearity in the control surface hinge. To understand the nonlinear aeroelastic characteristics, linear flutter analysis must be performed first. In the present study, the finite element method[11] is used for the free vibration analysis and doublet-hybrid method (DHM)[12,13] is used for the computation of subsonic unsteady aerodynamic forces. The methods of Roger[14] and Abel[15] are used to approximate the frequency-domain aerodynamic forces. The fictitious mass (FM) method by Karpel and Newman[16] and Karpel[17] is used to reduce the problem size and the computation time requirement. The effects of the hinge stiffness and the vibration characteristics of the control surface on the linear and nonlinear aeroelastic characteristics of a fighter-type wing are investigated.

Linear and Nonlinear Aeroelastic Analysis

Aeroelastic Equation

The aeroelastic equation with a concentrated structural nonlinearity can be written as

$$[M]\{\ddot{u}\} + [C]\{\dot{u}\} + [K_n(u)]\{u\} = \{F(t, u, \dot{u})\} \tag{1}$$

where $\{F\}$ is the aerodynamic force vector. For a piecewise nonlinearity, the restoring force term $[K_n(u)]\{u\}$ can be written as follows:

$$[K_n(u)]\{u\} = [K]\{u\} + \{f(u)\} \tag{2}$$

where $[K]$ is a linear stiffness matrix without a structural nonlinearity and $\{f(u)\}$ is the restoring force vector whose elements are zero except for the nonlinear contribution.

Fictitious Mass Method

Generally, aeroelastic analysis is conducted in generalized modal coordinates to save computational time and memory. In an aeroelastic system with structural nonlinearities, structural properties vary

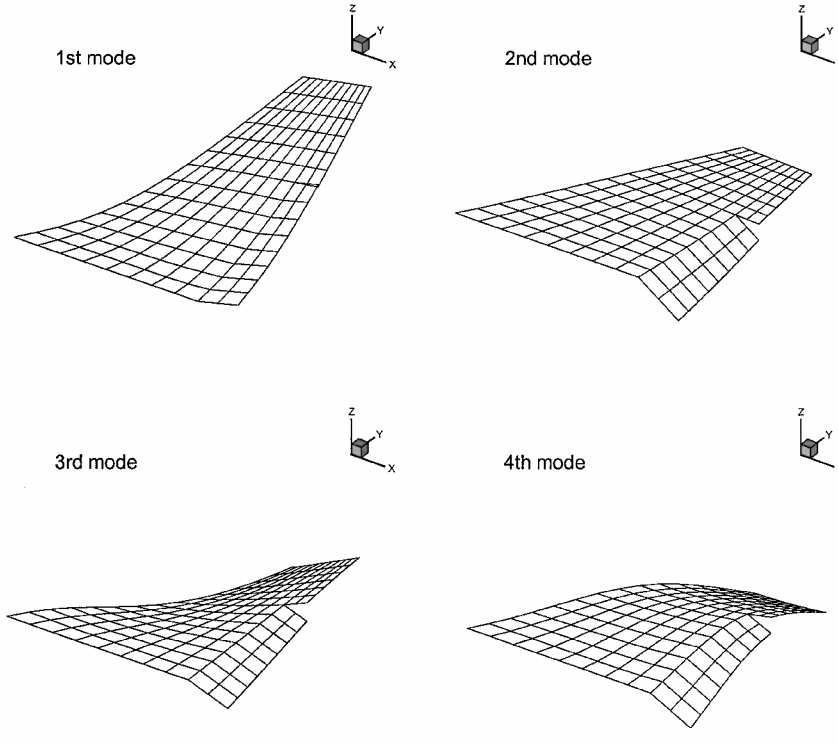

Fig. 3 Natural mode shapes, $K_\theta = 100$ N · m/rad.

with motion. Hence, aeroelastic analysis using the constant modal coordinates of the nominal structure can give inaccurate results and may require a relatively large number of modes to achieve a reasonable level of accuracy. Karpel and Newman[16] and Karpel[17] proposed the FM method to overcome this problem. In this method, FMs are added to the degrees of freedom (DOF) of the mass matrix where the structural variations will occur. The basic idea of the FM method is that the local deformation due to the large mass enables us to examine the structural variation, and the FM method provides an efficient and easy to apply computational scheme.

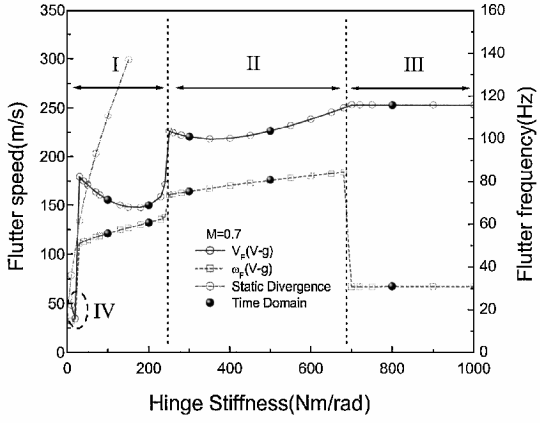

Fig. 4 Aeroelastic characteristics for various hinge stiffnesses.

The free vibration equations of motion of an n-DOF system loaded with FMs is given as

$$[M + M_f]\{\ddot{u}\} + [K]\{u\} = \{0\} \tag{3}$$

The elements of the FM matrix $[M_f]$ are zero except for the DOF where structural variations occur. The normal mode analysis of Eq. (3) provides a set of n_f low-frequency fictitious mass modes $[\phi_f]$. Then, the generalized mass and stiffness matrices are given as

$$[GM_f] = [\phi_f]^T[M + M_f][\phi_f]$$

$$[GK_f] = [\phi_f]^T[K][\phi_f] = [\omega_f]^2[GM_f] \tag{4}$$

where $[\omega_f]$ is a diagonal matrix of the natural frequencies, including zero frequencies for rigid-body modes. When the FM modes ($\{u\} = [\phi_f]\{\xi\}$) are used, the free vibration equations of motion of an actual structure whose stiffness matrix differs from those of the nominal structure by $[\Delta K]$ can be rewritten as

$$\left([GM_f] - [\phi_f]^T[M_f][\phi_f]\right)\{\ddot{\xi}_f\}$$

$$+ \left([GK_f] + [\phi_f]^T[\Delta K][\phi_f]\right)\{\xi_f\} = \{0\} \tag{5}$$

The mode shapes of the FM model are transformed to the basic structure by using the following relation:

$$[\phi_b] = [\phi_f][\chi_b] \tag{6}$$

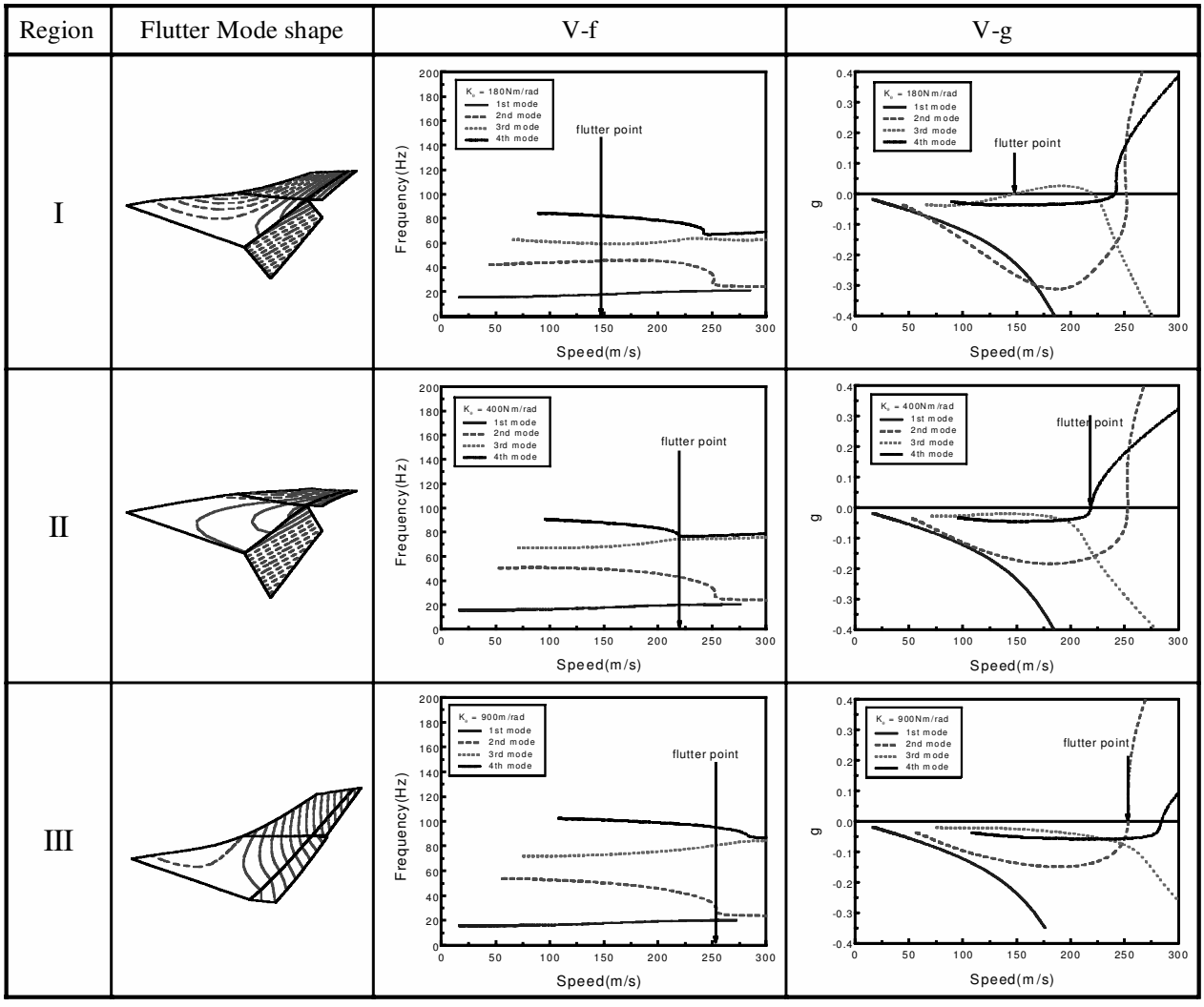

Fig. 5 Flutter mode shapes, *V–f* and *V–g* diagrams.

where $[\chi_b]$ are the eigenvectors associated with Eq. (5). The basic mode shapes $[\phi_b]$ serve as a constant set of structural generalized coordinates throughout the aeroelastic analysis.

Method of Aeroelastic Analysis

The aeroelastic analysis can be subdivided into two methods. One is frequency-domain analysis such as a $V-g$ method (KE method[11]) or $P-K$ method.[11] The other is time-domain analysis such as the time integration of Eq. (1). Frequency-domain and time-domain methods have different approaches, but these methods give similar solutions for a linear aeroelastic problem.

The frequency-domain analysis has the advantages of relatively less computation time, simplicity of the analysis procedure, and ease of physical interpretation. However, this method can not be directly applied to an aeroelastic problem with structural nonlinearities. To overcome this disadvantage, these nonlinearities should be linearized by a method such as a describing function method. The advantage of time-domain analysis is that this method can be applied to both linear and nonlinear problems, but the disadvantages are relatively more computation time, complexity of analysis procedure, and difficulty of physical interpretation. Therefore, aeroelastic analysis with structural nonlinearities should be performed by using both methods for an effective and accurate analysis.

***V–g* Method**

When the modal matrix $[\phi_b]$ obtained from the FM model is used, the structural displacements can be transformed into modal coordinates as follows:

$$\{u\} = [\phi_b]\{u\} \tag{7}$$

where $\{u\}$ is the displacement in modal coordinates. Then, the generalized aerodynamic forces can be written as

$$\{F\} = [\phi_b]^T\{F\} = q[\phi_b]^T[Q][\phi_b]\{u\} = q[Q]\{u\} \tag{8}$$

where $q(=\frac{1}{2}\rho U^2)$ and $[Q]$ are a dynamic pressure and the generalized aerodynamic coefficient matrix, respectively.

When the damping and the nonlinear terms in Eq. (1) are ignored and the transformation in Eq. (7) is used, the aeroelastic equation in Eq. (1) can be transformed into the generalized coordinate as follows:

$$[GM]\{\ddot{u}\} + [GK]\{u\} = q[Q]\{u\} \tag{9}$$

From the FM modal approach,[16,17] the generalized mass matrix $[GM]$ and the generalized stiffness matrix $[GK]$ are defined as

$$[GM] = [GM_f] - [\phi_b]^T[M_f][\phi_b] \tag{10}$$

$$[GK] = [GK_f] + [\phi_b]^T[\Delta K][\phi_b] \tag{11}$$

If the motion is harmonic ($\{u\} = \{\bar{u}\}e^{i\omega t}$), then Eq. (9) can be written as

$$(-\omega^2[GM] - q[Q(k)] + [GK])\{\bar{u}\} = \{0\} \tag{12}$$

When the reduced frequency $k(=\omega b/U)$ is used, Eq. (12) is finally rewritten as

$$\left\{-(k^2/b^2)[GM] - \tfrac{1}{2}\rho[Q(k)] + (1/U^2)[GK]\right\}\{\bar{u}\} = \{0\} \tag{13}$$

The artificial structural damping is introduced into the flutter equation in Eq. (13) to use the $V-g$ method. When $[GK]$ is substituted by $(1+ig)[GK]$, Eq. (13) becomes

$$\left\{-(k^2/b^2)[GM] - \tfrac{1}{2}\rho[Q(k)] + \lambda[GK]\right\}\{\bar{u}\} = \{0\} \tag{14}$$

where λ is defined as

$$\lambda = (1+ig)/U^2 \tag{15}$$

Finally, Eq. (14) can be rewritten as follows:

$$\lambda\{\bar{u}\} = [A]\{\bar{u}\} \tag{16}$$

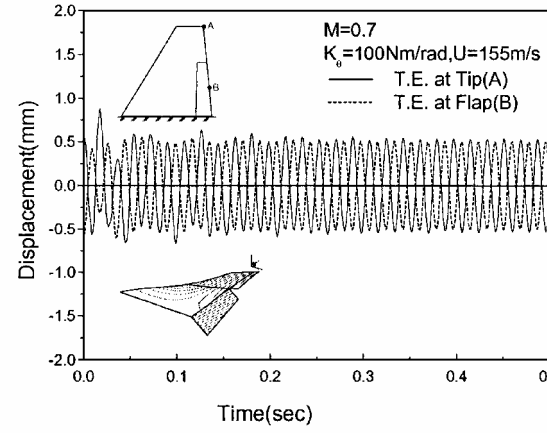

Region I

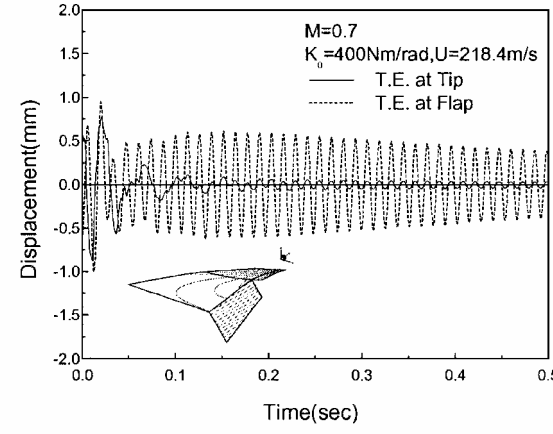

Region II

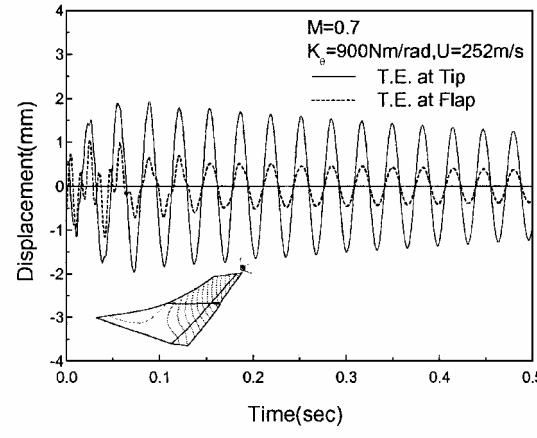

Region III

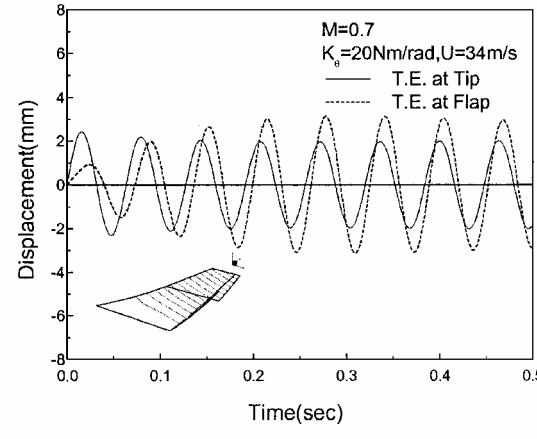

Region IV

Fig. 6 Aeroelastic responses at the vicinity of the flutter speed.

where

$$[A] = [GK]^{-1}\left\{(k^2/b^2)[GM] + \tfrac{1}{2}\rho[Q(k)]\right\} \tag{17}$$

Then, Eq. (16) becomes a complex eigenvalue problem, and matrix $[A]$ is a function of k. For various values of k, here λ are obtained by solving the eigenvalue problem of Eq. (16). From the definition of λ, the speed, structural damping, and frequency are calculated as follows:

$$U = \sqrt{1/\mathrm{Re}(\lambda)}, \qquad g = \mathrm{Im}(\lambda)/\mathrm{Re}(\lambda)$$

$$\omega = (1/2\pi)(Uk/b) \tag{18}$$

As the speed increases, the structural damping g changes from negative to positive. This point is the flutter point; the speed U is the flutter speed U_f, and the frequency ω is the flutter frequency ω_f.

Time-Integration Method

To integrate the aeroelastic equations in Eq. (1), Eq. (1) may be transformed into state-space equations. Generally, the generalized aerodynamic influence coefficients are calculated for reduced frequencies k by unsteady aerodynamic methods such as panel methods (doublet-point method[12] or DHM[13]). Thus, the generalized aerodynamic influence coefficients should be approximated by a rational function for the time-domain analysis. There are many methods for rational function approximation (RFA), such as Roger's RFA[14] and Karpel's minimum-state approximation.[18] Roger's RFA is used here. The approximation form of Roger's method is as follows:

$$[Q(k)] = [A_1] + [A_2](ik) + [A_3](ik)^2 + \sum_{m=4}^{7} \frac{[A_m](ik)}{(ik) + \beta_m} \tag{19}$$

where A_i are calculated from a least-square fit and β_m are the aerodynamic poles and constants to be determined for best fit of $[Q]$.

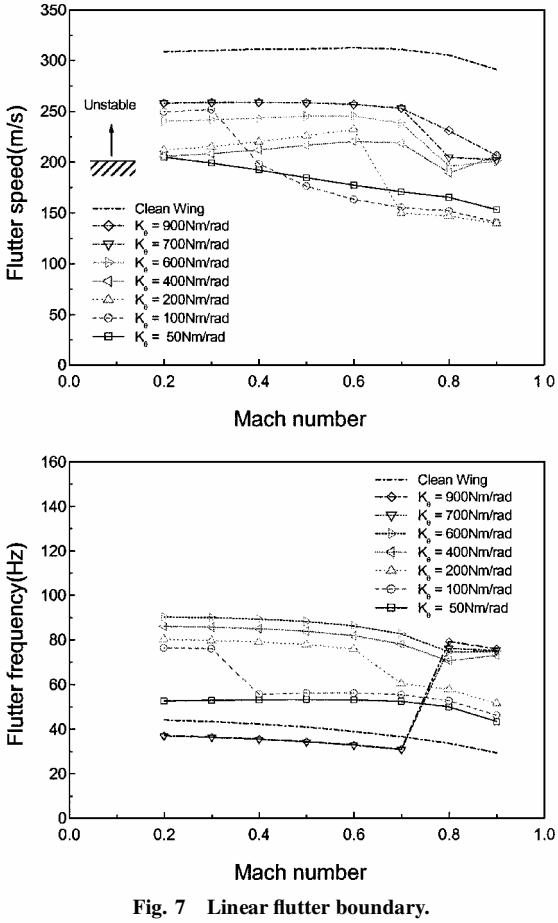

Fig. 7 Linear flutter boundary.

When this approximation is used, the final state-space aeroelastic equations are obtained as

$$\begin{Bmatrix} \{\dot{v}\} \\ \{\dot{u}\} \\ \{\dot{z}_4\} \\ \vdots \\ \{\dot{z}_7\} \end{Bmatrix} = \begin{bmatrix} [\hat{C}] & [\hat{K}] & [\hat{A}_4] & \cdots & [\hat{A}_7] \\ [I] & [0] & [0] & \cdots & [0] \\ [0] & [I] & -p_4[I] & \cdots & [0] \\ \vdots & \vdots & \vdots & \ddots & \vdots \\ [0] & [I] & [0] & \cdots & -p_7[I] \end{bmatrix} \begin{Bmatrix} \{v\} \\ \{u\} \\ \{z_4\} \\ \vdots \\ \{z_7\} \end{Bmatrix}$$

$$-[\hat{M}]^{-1} \begin{Bmatrix} [\phi]^T\{f(u)\} \\ [0] \\ [0] \\ \vdots \\ [0] \end{Bmatrix} \tag{20}$$

where

$$\{v\} = \{\dot{u}\} \tag{21a}$$

$$\{\dot{v}\} = \{\ddot{u}\} \tag{21b}$$

$$[\hat{M}] = [GM] - q\left(\frac{b}{U}\right)^2 [A_3] \tag{21c}$$

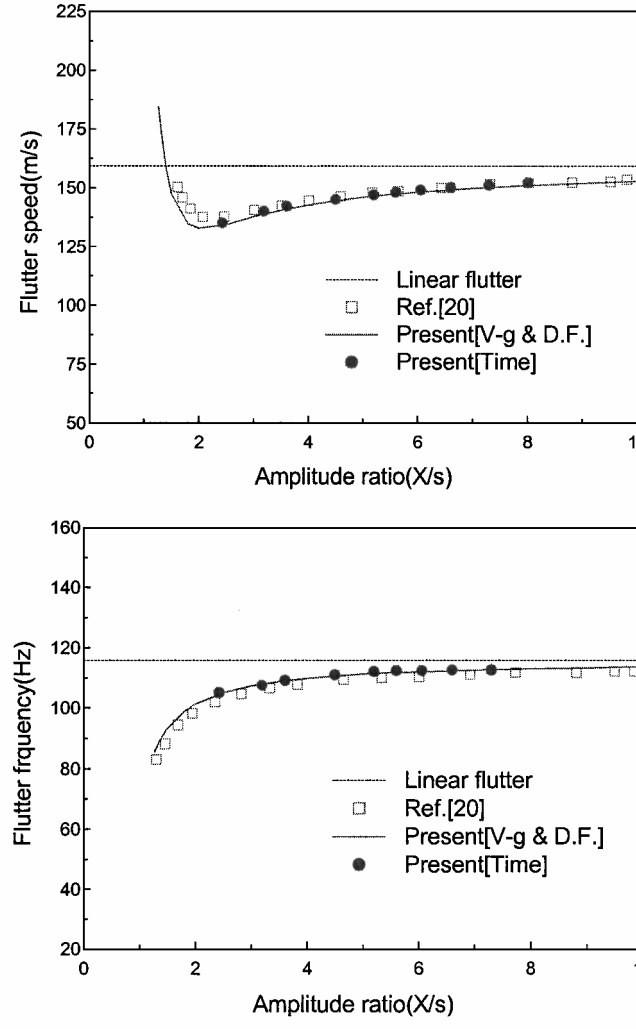

Fig. 8 Nonlinear flutter results of missile control fin with free-play nonlinearity.

$$[\hat{C}] = -[\hat{M}]\left([GM] - q\left(\frac{b}{U}\right)[A_2]\right) \tag{21d}$$

$$\lfloor \hat{K} \rfloor = -\lfloor \hat{M} \rfloor([GK] - q[\bar{A}_1]) \tag{21e}$$

$$\lfloor \hat{A}_m \rfloor = -qp_m \lfloor \hat{M} \rfloor [A_m] \tag{21f}$$

$$[\bar{A}_1] = [A_1] + \sum_{m=4}^{7} [A_m] \tag{21g}$$

$$p_m = \beta_m\left(\frac{b}{U}\right) \tag{21h}$$

In this paper, the fourth-order adaptive Runge–Kutta method (see Ref. 19), with step doubling and adaptive step size control schemes, is used to integrate Eq. (20).

Results and Discussion

As a numerical example, a fighter-type wing with a control surface is used for linear and nonlinear aeroelastic analyses. The model configuration is shown in Fig. 1. The material used in this analysis is aluminum. The material properties of the aluminum are $E = 72$ GPa, $\rho = 2700\,\text{kg/m}^3$, and $\nu = 0.33$, and the thickness of the wing is 6 mm.

Free Vibration Analysis

The finite element method[11] is used for the free vibration analysis of a fighter-type wing. For the FM, 140 (14×10) four-node shell elements, one one-dimensional spring element for a hinge spring, and one mass element ($10\ \text{kg} \cdot \text{m}^2$) are used. Table 1 shows the natural frequencies of the fighter-type wing with the control surface using both the direct method and FM method. With the direct method, the fighter-type wing is directly modeled with a hinge spring, whereas with the FM method, wing is modeled with an FM and without a hinge spring. Through the free vibration analysis, the FM model is established by using Eq. (5). Natural frequencies of the FM model are in good agreement with those of the direct model except for the highest modes. This is because an added FM causes local distortion in the highest mode.[16,17] Figure 2 shows the variations of the first four natural frequencies with value of hinge stiffness, and Fig. 3 shows the mode shapes. When a hinge stiffness is $100\ \text{N} \cdot \text{m/rad}$, the

Table 1 Comparison of natural frequencies ($K_\theta = 100\ \text{N} \cdot \text{m/rad}$)

Mode no.	Direct method	FM method				
		4	6	8	10	12
1	15.64	15.64	15.64	15.64	15.64	15.64
2	33.48	33.89	33.50	33.49	33.48	33.48
3	62.25	63.12	62.28	62.26	62.25	62.25
4	83.71	90.76	83.81	83.73	83.71	83.71
5	164.52		165.24	164.68	164.53	164.53
6	213.39		333.28	214.39	213.47	213.44
7	283.83			287.43	284.07	283.99
8	319.38			478.51	320.16	319.86
9	387.73				387.87	387.80
10	429.02				1089.02	429.03
11	490.83					491.33
12	552.97					1180.06

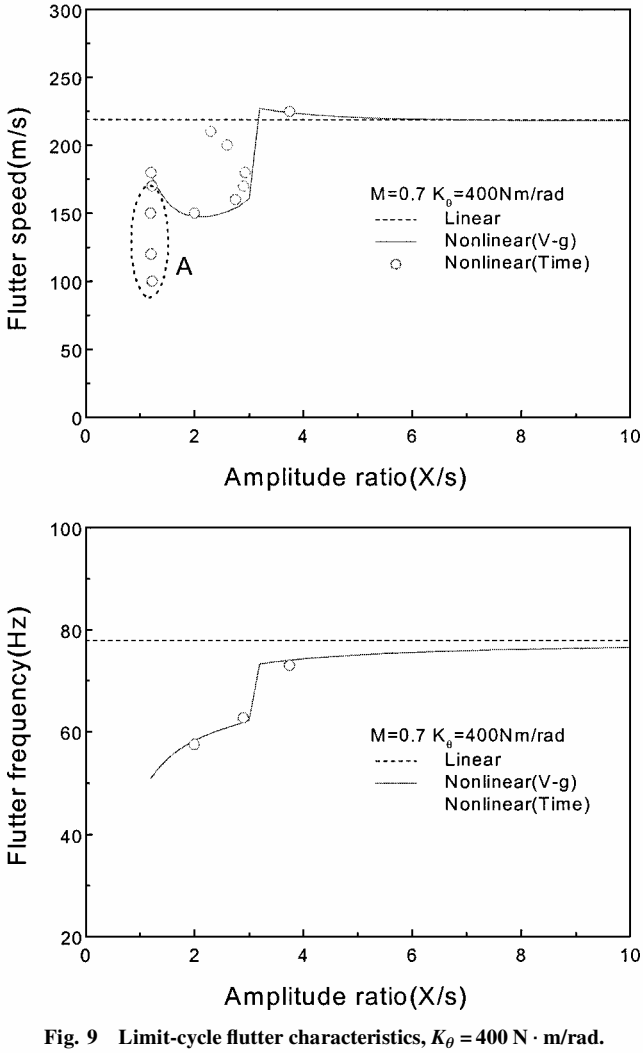

Fig. 9 Limit-cycle flutter characteristics, $K_\theta = 400\ \text{N} \cdot \text{m/rad}$.

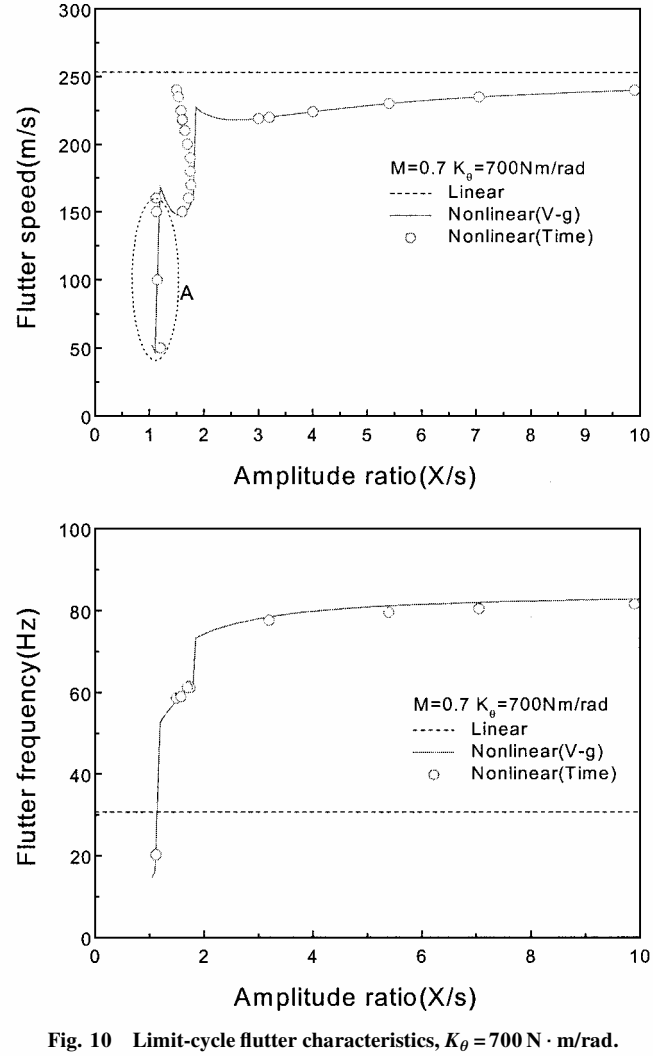

Fig. 10 Limit-cycle flutter characteristics, $K_\theta = 700\ \text{N} \cdot \text{m/rad}$.

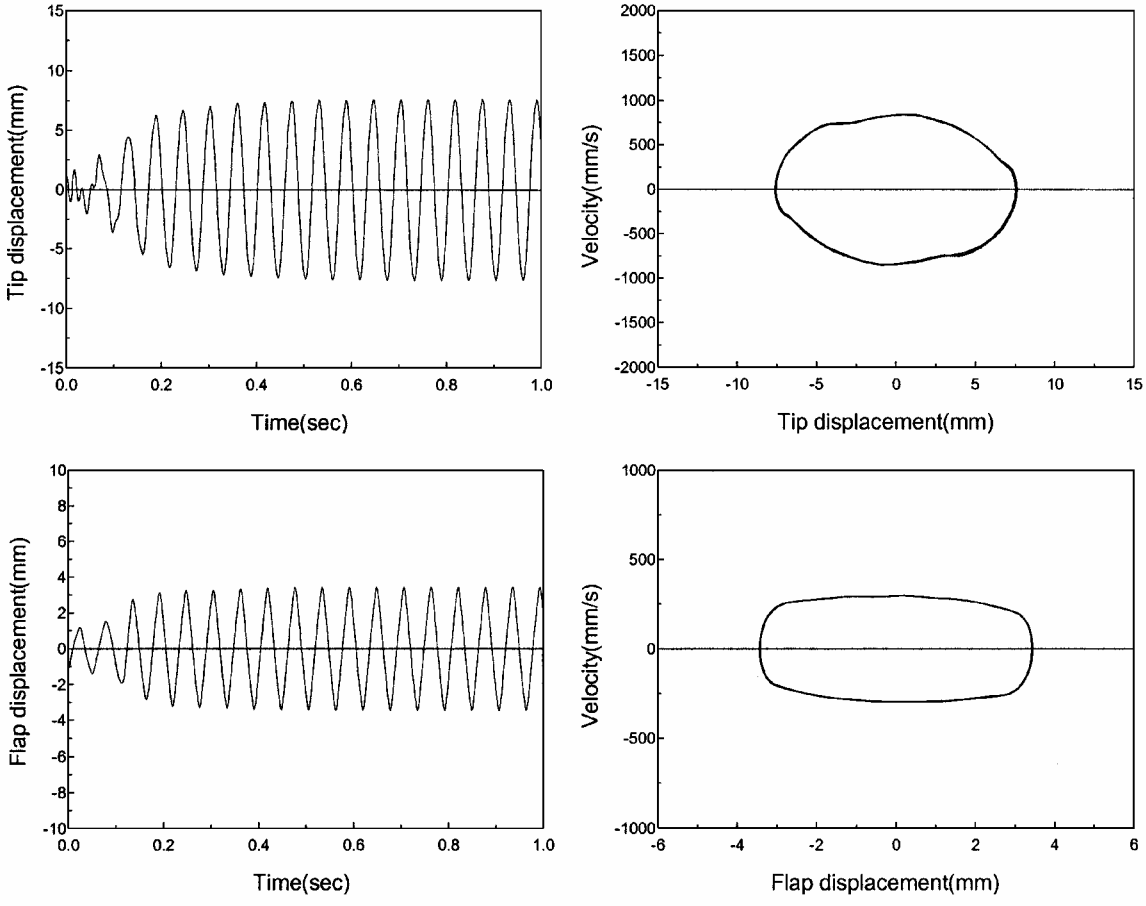

Fig. 11 Time history and phase plot in region A of Fig. 9; $M = 0.7$, $K_\theta = 400$ N · m/rad, and $U = 100$ m/s.

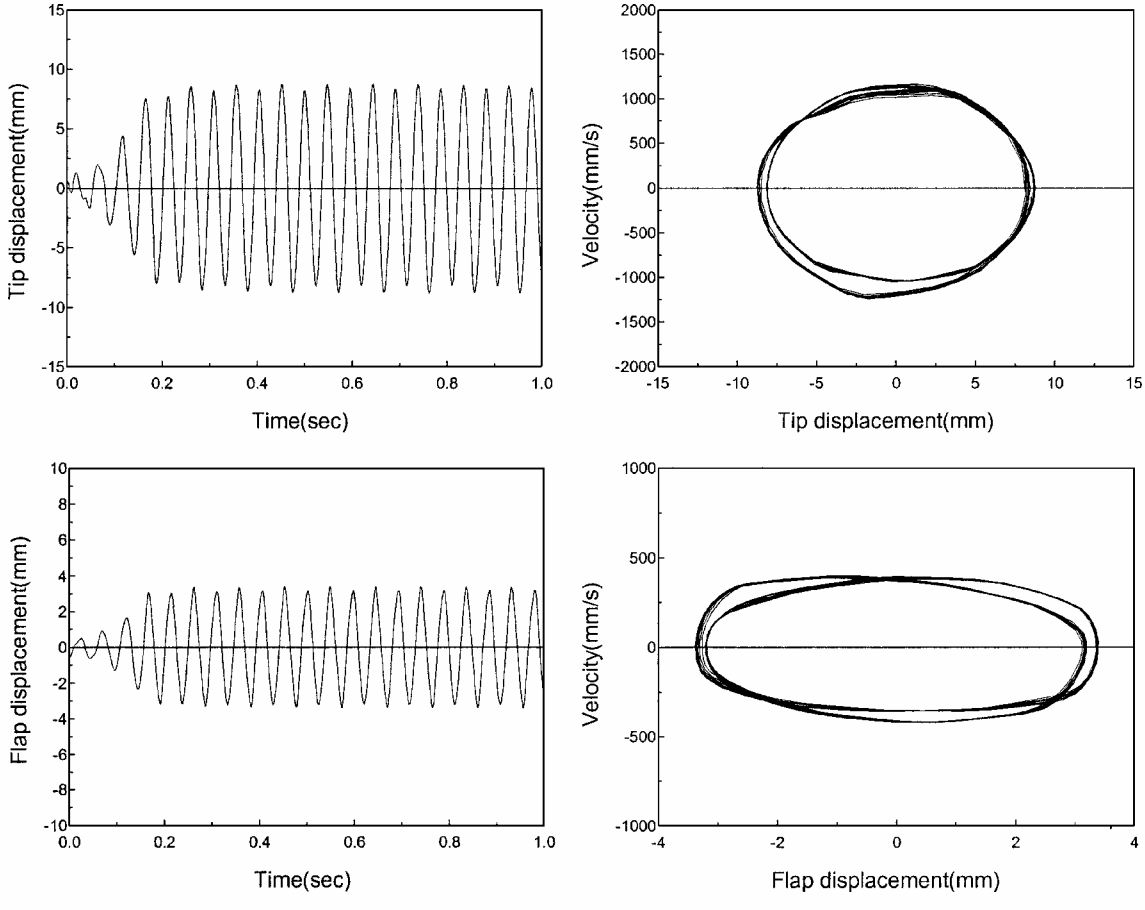

Fig. 12 Time history and phase plot, $U = 170$ m/s and $\theta_0 < s$.

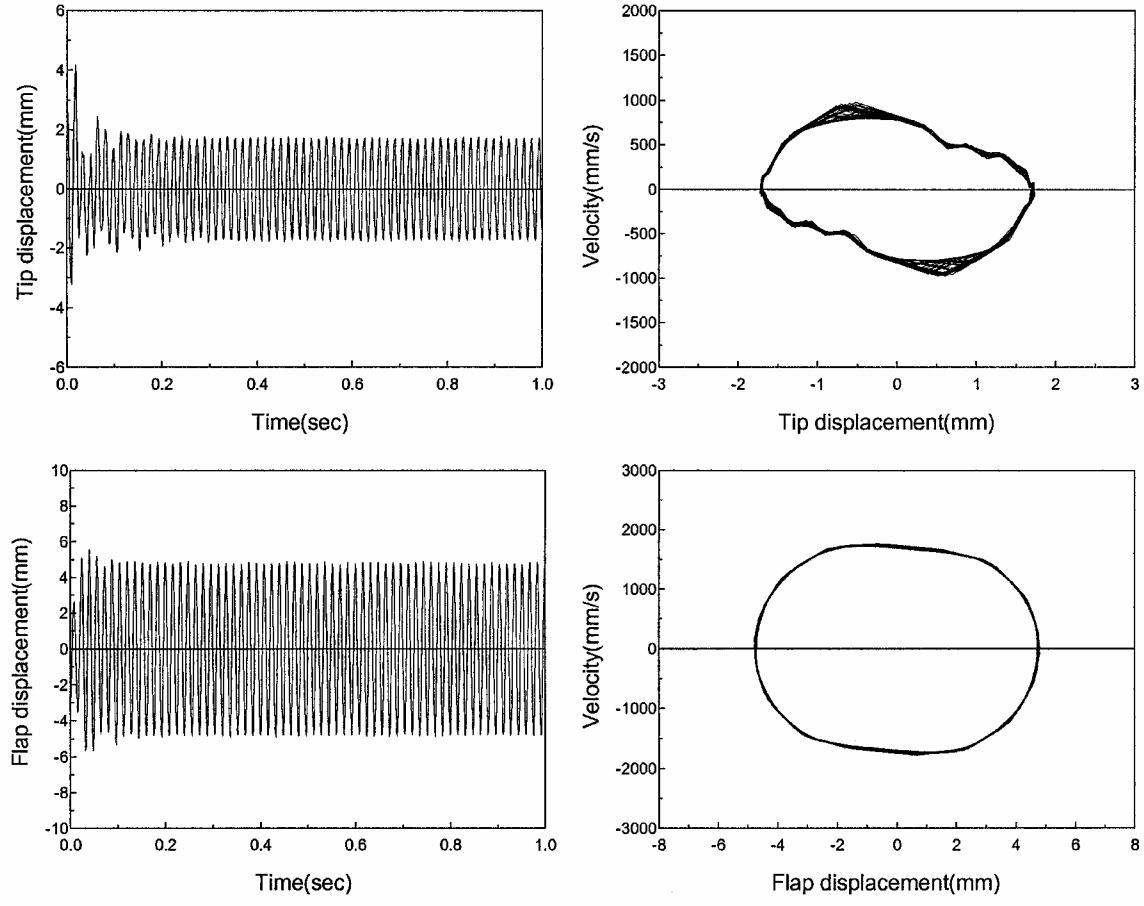

Fig. 13 Time history and phase plot, $U = 170$ m/s and $\theta_0 > s$.

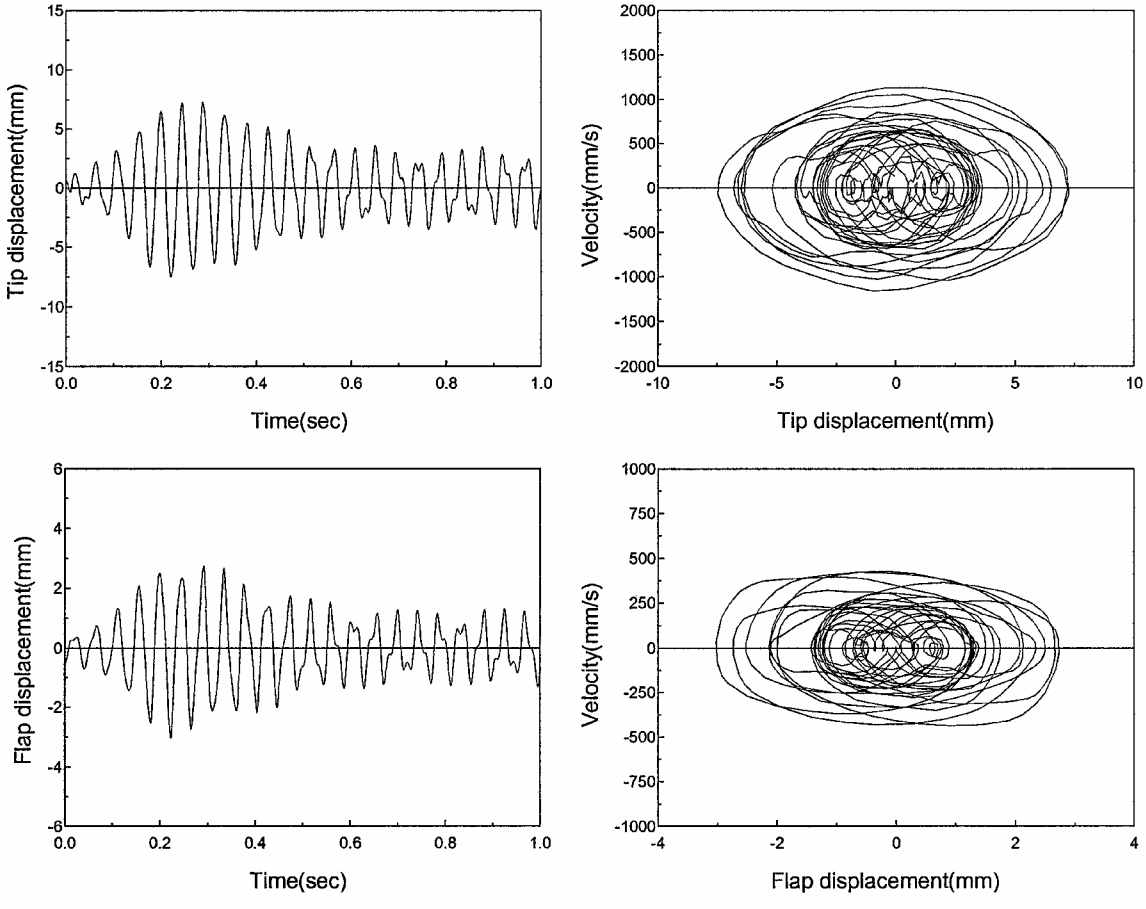

Fig. 14 Time history and phase plot, $U = 190$ m/s and $\theta_0 < s$.

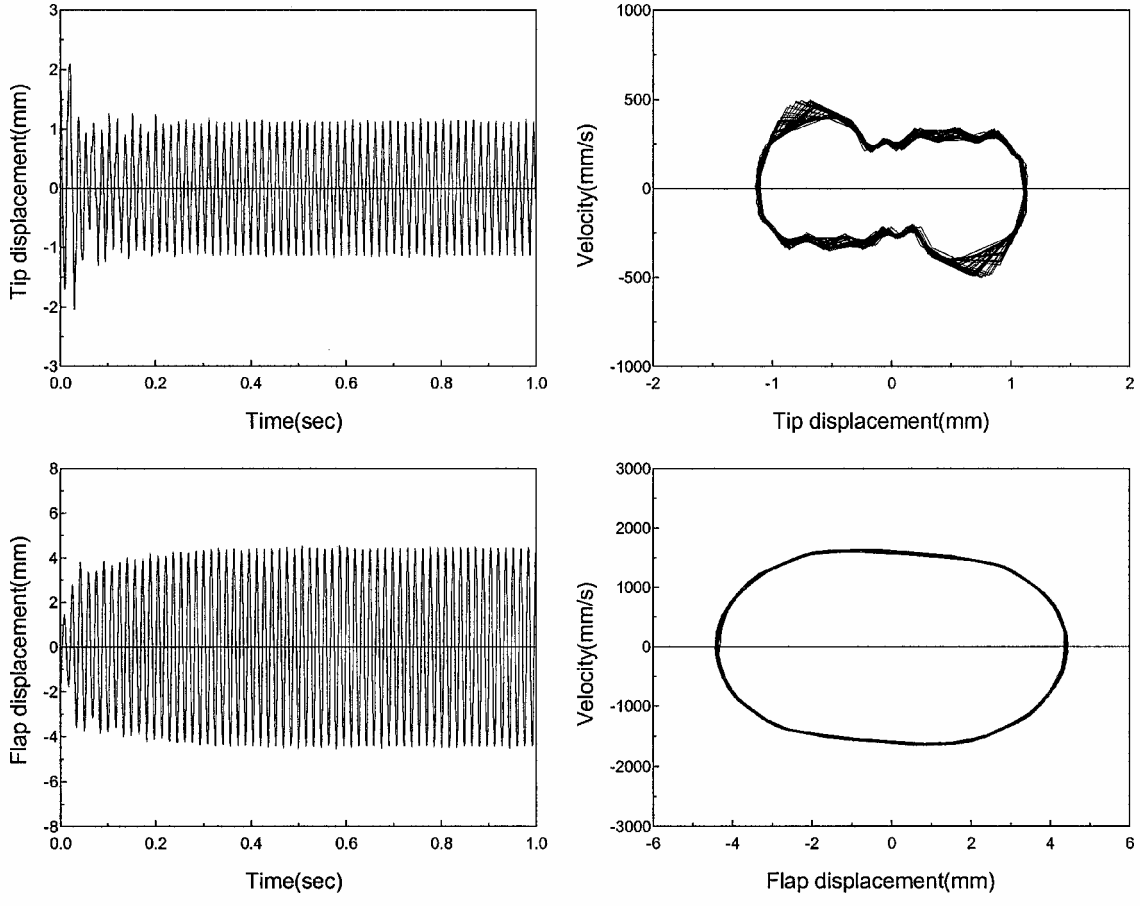

Fig. 15 Time history and phase plot, $U = 190$ m/s and $\theta_0 > s$.

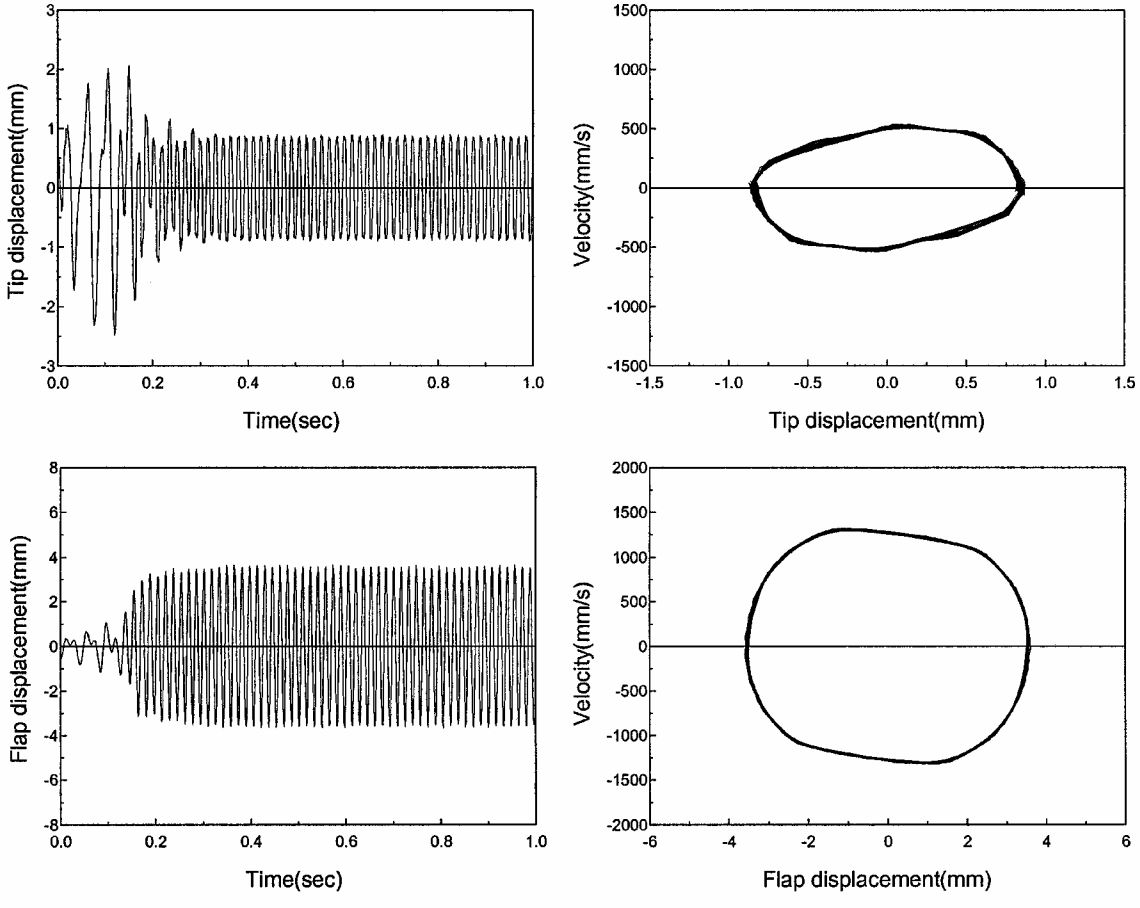

Fig. 16 Time history and phase plot, $U = 210$ m/s and $\theta_0 < s$.

first mode is the first bending mode and the second is the flapping mode of control surface. The third and fourth modes are the first torsion and the second bending modes, respectively. The mode shapes for other hinge stiffness are similar except for the interchange between the first mode and the second mode. Near the hinge stiffness of 20 N · m/rad, an exchange of natural modes occurs in the first and second modes. Because of this exchange, the flutter speed is remarkably decreased. As the hinge stiffness is varied, the natural frequency of the second mode is varied significantly.

Linear Aeroelastic Analysis

The DHM code is used to compute the subsonic unsteady aerodynamic forces, and the mesh of the aerodynamic grid is 15 × 15. To verify the computational scheme and program in the present study, the hinge stiffness of the control surface used is 100 N · m/rad, and the number of modes used for the aeroelastic analysis is eight. The results of the present aeroelastic analysis are compared with those of Ref. 11, where the DLM and *KE* methods were used. The comparison of the flutter speed and frequency between $V-g$ and other methods is shown in Table 2. The results of the $V-g$ method, root-locus method, and time-integration method are in good agreement with those of Ref. 11, and the flutter speed of a fighter-type wing with control surface is remarkably decreased compared with that of a clean wing, which is the wing without a control surface. The results of the FM method are very accurate compared with those of the direct method.

The variation of the flutter speed and frequency is shown in Fig. 4. Figure 4 shows that the flutter speed and frequency vary considerably for the variation of hinge stiffness and that there exist values of stiffness at which the abrupt change of the flutter frequency occurs. This is due to the change of the flutter modes. The flutter characteristics with hinge stiffness effects can be characterized by four regions by the flutter mode shapes. Hinge stiffness effects in region IV are very small, and the flutter type is bending–flapping mode flutter. Region IV is not as important except for the case in which the hinge fails; thus, this region is ignored in the linear aeroelastic analysis. However, region IV is important in the nonlinear aeroelastic analysis, and this region will be presented later.

Figure 5 shows the flutter mode shapes, $V-f$ plots, and $V-g$ plots for three regions in Fig. 4. The flutter mode shapes represent the magnitudes of the complex flutter modes. The flutter types of regions I, II and III are the hump mode flutter of the third mode, the third–fourth mode (first torsion–second bending) coalescence flutter, and the first–second mode (first bending–first torsion) coalescence flutter. The flutter type of region III is typically mode coalescence flutter of a clean wing. The flutter mechanism of regions I and II originates from the flapping mode of the control surface and is important

Table 2 Comparison of flutter speeds and frequencies (K_θ = 100 N · m/rad)

Method	Flutter speed, m/s	Flutter frequency, Hz
$V-g$ (direct)	175.61	55.99
Time (direct)	176.20	56.15
$V-g$ (FM)	176.31	56.01
Root locus (FM)	176.37	56.00
Time (FM)	176.60	56.15
NASTRAN (*KE*, DLM)	177.25	56.51
	Clean wing	
Present ($V-g$, DHM)	312.74	40.71
NASTRAN (*KE*, DLM)	311.45	40.92

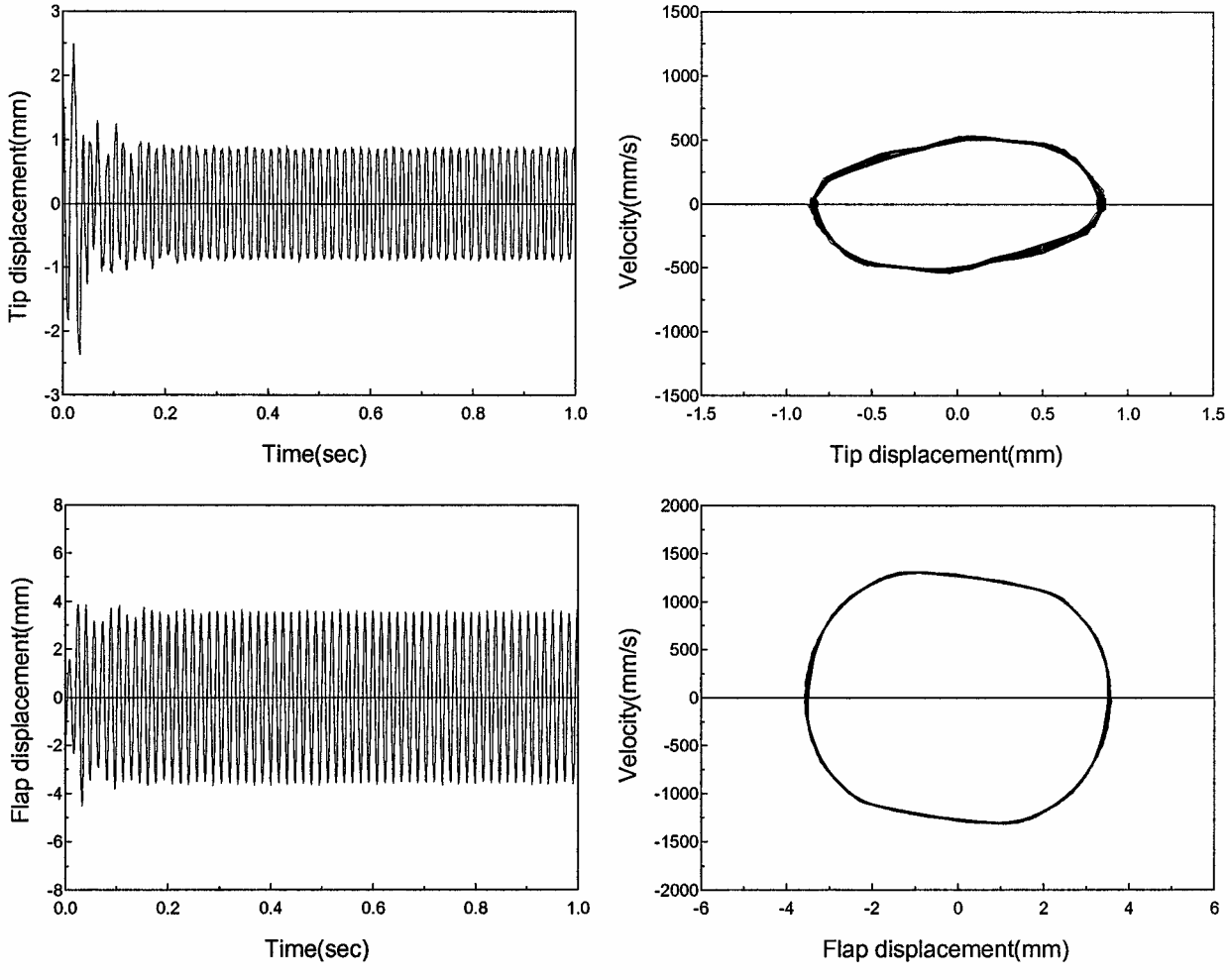

Fig. 17 Time history and phase plot, U = 210 m/s and $\theta_0 > s$.

in the aeroelasticity of the wing with a control surface. Figure 6 shows the aeroelastic responses at the vicinity of the flutter speed. The responses are quite different, depending on the hinge stiffness. Figure 7 shows the linear flutter boundary. The linear flutter boundary is much lower than that of a clean wing, and the flutter speed and frequency vary considerably with changes in the hinge stiffness.

Nonlinear Aeroelastic Analysis

In the present study, the nonlinearity of the hinge stiffness is represented by the free-play nonlinearity. For a free-play nonlinearity, the restoring force in Eq. (2) can be written as

$$f(u) = \begin{cases} K_\theta(u - s), & u > s \\ 0, & -s < u < s \\ K_\theta(u + s), & u < -s \end{cases} \tag{22}$$

where s is a free-play angle. For the frequency-domain analysis, the describing function method is used, and the restoring force in Eq. (22) can be linearized as

$$f(u) = \delta u \tag{23}$$

$$\delta = \begin{cases} 0, & 0 < X < s \\ (K_\theta/\pi)\{\pi - 2\sin^{-1}(s/X) \\ \quad - \sin[2\sin^{-1}(s/X)]\}, & X > s \end{cases} \tag{24}$$

where X is the amplitude of LCO. Equations (23) and (24) are used for the V–g method, and Eq. (22) is used for the time-integration method. Figure 8 shows the nonlinear flutter results of a missile control fin with free-play nonlinearity.[20] The results of Ref. 20 shown in Fig. 8 are calculated by using the V–g method with a describing function. The present results are in good agreement with those of Ref. 20.

Figures 9 and 10 show the LCO flutter characteristics when the hinge stiffness is 400 N/m and 700 N · m/rad, respectively. The results of the V–g method and the time-integration method agree well each other. LCOs, which can not be observed in the frequency-domain analysis, are observed in the time-domain analysis. In Figs. 9 and 10, LCOs with two or more periods and chaotic motion are not presented. The LCO characteristics are similar to the linear flutter characteristics in Fig. 4. The LCOs are caused by the equivalent stiffness of a free-play spring related to the LCO amplitude ratio (X/s) of the hinge angle. Figures 9 and 10 show that two types of LCO are observed for air speeds below the linear flutter boundary. One type is a small-amplitude LCO, and the other type is a large-amplitude LCO. These motions are classified by the amplitude of the hinge angle and are dependent on the initial amplitude of the hinge angle. The LCOs of region A in Figs. 9 and 10 have very small amplitudes and are observed in the range of very low air speed. Region A is similar to region IV in Fig. 4. When the hinge stiffness is 400 N · m/rad, the flutter speed of the nonlinear case becomes higher than that of the linear case. However, the case when the hinge stiffness is 700 N · m/rad does not become higher. LCOs are very important because they are observed for air speeds below the linear flutter boundary.

The time history and phase plot at wing tip and flap are shown in Figs. 11–17. The geometry for the wing tip and flap is same as in Fig. 6. Figure 18 shows two types of the LCO mode shapes. The value of the free-play angle s used is 1.0 deg. The Mach number is 0.7, and the hinge stiffness is 400 N · m/rad. The initial conditions considerably affect the stability of a nonlinear system, and any mode may go unstable due to initial conditions. However, the initial conditions used in Figs. 11–17 are sufficiently small so that any mode does not go unstable. Figure 11 shows that the LCOs of region A of Fig. 9 are observed at low speed. The amplitude of a hinge angle is small but that of a tip displacement is large compared with other cases because the LCO mode is the bending–flapping coalescence mode shown in Fig. 18a. Figures 12 and 13 show two types of LCO when the air speed is 170 m/s. When the initial condition θ_0 is less than the free-play angle s, the motion goes to the small-amplitude LCO. Conversely, when θ_0 is greater than s, the motion goes to the large-amplitude LCO. The flutter mode of the former is the same as that in Fig. 11 and that of the latter is the torsion–flapping coalescence mode shown in Fig. 18b. Figures 14 and 15 show the aeroelastic responses for the case of air speed of 190 m/s. Chaotic motion is observed when θ_0 is less than s, and LCO is observed when θ_0 is greater than s. Chaotic motion occurs through coupling of the bending, flapping, and torsion modes. Figures 16 and 17 show LCOs for the case of air speed of 210 m/s. At this air speed, an LCO that has only one amplitude is observed, and the amplitude of this LCO is independent of the initial conditions. This LCO can not be observed in the frequency-domain analysis, as shown in Fig. 9. LCO characteristics for the case when the hinge stiffness is 700 N · m/rad are similar to the case when the hinge stiffness is 400 N · m/rad, but the flutter speed is lower than that of the linear case. Figure 19 shows the LCO amplitudes of the wing tip and flap displacements for various air speeds below the linear flutter speed U_{ref} when the hinge stiffness is 400 N · m/rad. For air speeds between 0 and approximately 30% of the linear flutter speed, LCO is not observed, and the oscillation damps out to zero. For air speeds between approximately 60 and 80%, LCOs with two or more periods and chaotic motions are observed. The bending–flapping mode LCO between approximately 30 and 60% of the linear flutter speed must be considered because the amplitude is large compared with other LCOs. Jumps of

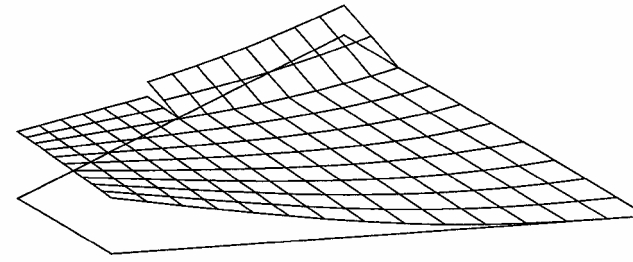

a) Bending–flapping mode LCO

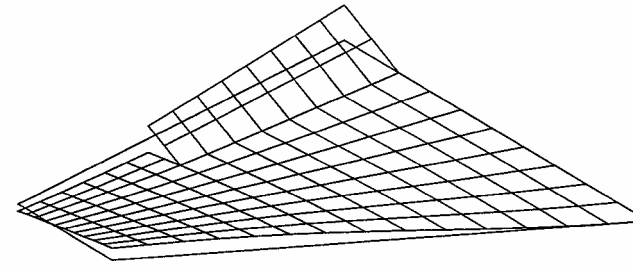

b) Torsion–flapping mode LCO

Fig. 18 LCO flutter mode shapes.

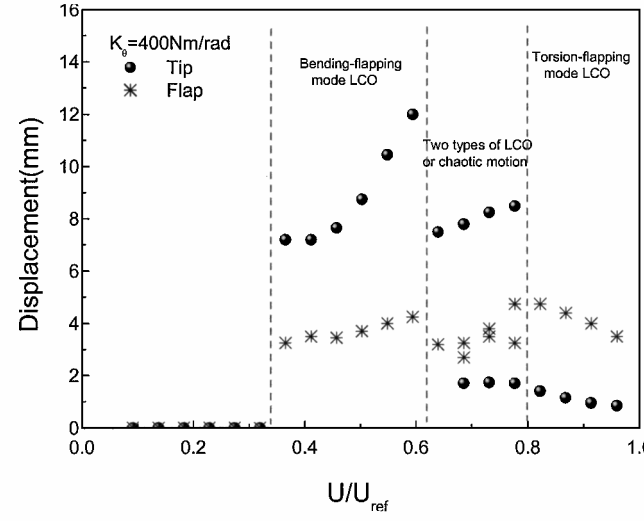

Fig. 19 LCO amplitudes of tip and flap displacements for various air speed, K_θ = 400 N · m/rad and U_{ref} = 219 m/s.

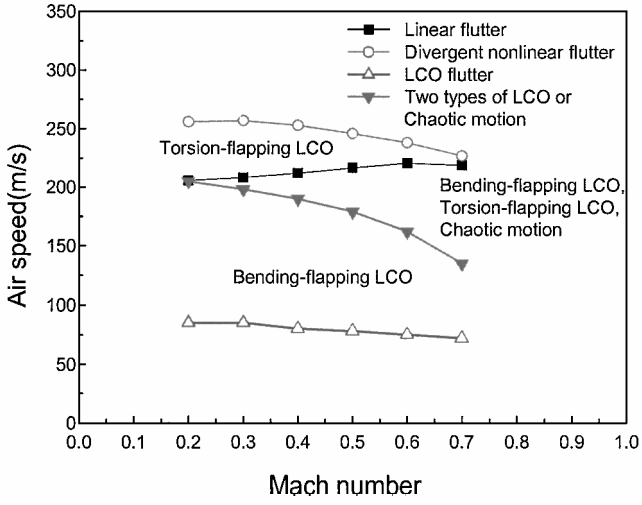

Fig. 20 Nonlinear flutter boundary, $K_\theta = 400$ N · m/rad.

LCO amplitudes are observed at approximately 60% (as observed in Ref. 10). This is caused by the change of the LCO mode shape. Typically, this jump is not observed in other nonlinear aeroelastic studies and is caused by the nonlinear flutter mode shapes, especially the flapping mode of the control surface. Figure 20 shows the nonlinear flutter boundary when the hinge stiffness is 400 N · m/rad. The bending–flapping mode LCO is observed at air speeds below the linear flutter speed. The nonlinear flutter speed is higher than that of the linear flutter speed for the case of 400 N · m/rad. Chaotic motion is also observed in the range of air speed below or over the linear flutter speed.

Conclusions

Linear and nonlinear aeroelastic analyses of the fighter-type wing with a control surface are performed in the frequency domain and the time domain. The results of the free vibration analysis and linear flutter analysis support the validity of the present method. Nonlinearity of a hinge spring is represented by a free-play nonlinearity, and the describing function method is used for the frequency-domain analysis.

Linear flutter analysis shows that the flutter characteristics of the fighter-type wing with a control surface vary considerably with the hinge stiffness due to the presence of the flapping mode of the control surface. Nonlinear flutter analysis shows that LCOs are observed in a wide range of air speeds below the linear flutter boundary. As in the linear case, the flapping mode of the control surface affects the nonlinear flutter characteristics considerably. Time-domain analysis is used for the nonlinear flutter analysis because of the presence of LCO with two or more periods and chaotic motion, which can not be observed in the frequency-domain analysis. At the same air speed, two LCO types, with small and large amplitudes of hinge angle, are observed. Jumps of LCO amplitude are observed and are caused by the change of the nonlinear flutter mode shapes. In particular, we observe a change from a bending–flapping mode to a torsion–flapping mode. Thus, the flapping mode of the control surface must be considered within both linear and nonlinear flutter analyses.

Acknowledgments

This research was supported by the Agency for Defense Development and the Ministry of Science and Technology (National Research Laboratory Program) in the Republic of Korea. This support is gratefully acknowledged.

References

[1]Bisplinghoff, R. L., Ashley, H., and Halfman, R. L., *Aeroelasticity*, Addison–Wesley, Cambridge, England, U.K., 1955.

[2]Dowell, E. H., Crawley, E. F., Curtiss, H. C., Jr., Peters, D. A., Scanlan, R. H., and Sisto, F., *A Modern Course in Aeroelasticity*, Kluwer Academic, Norwell, MA, 1995.

[3]Shen, S. F., "An Approximate Analysis of Nonlinear Flutter Problems," *Journal of Aeronautical Sciences*, Vol. 26, Jan. 1959, pp. 25–32.

[4]Wooston, D. S., Runyan, H. W., and Andrews, R. E., "An Investigation of Effects of Certain Type of Structural Nonlinearities on Wing and Control Surface Flutter," *Journal of Aeronautical Sciences*, Vol. 24, Jan. 1957, pp. 57–63.

[5]Laurenson, R. M., and Trn, R. M., "Flutter Analysis of Missile Control Surface Containing Structural Nonlinearities," *AIAA Journal*, Vol. 18, No. 10, 1980, pp. 1245–1251.

[6]Lee, C. L., "An Iterative Procedure for Nonlinear Flutter Analysis," *AIAA Journal*, Vol. 24, No. 5, 1986, pp. 833–840.

[7]Lee, B. H. K., and Tron, A., "Effects of Structural Nonlinearities on Flutter Characteristics of the CF-18 Aircraft," *Journal of Aircraft*, Vol. 26, No. 8, 1989, pp. 781–786.

[8]Yang, Z. C., and Zhao, L. C., "Analysis of Limit Cycle Flutter of an Airfoil in Incompressible Flow," *Journal of Sound and Vibration*, Vol. 123, No. 1, 1988, pp. 1–13.

[9]Lee, I., and Kim, S. H., "Aeroelastic Analysis of a Flexile Control Surface with Structural Nonlinearity," *Journal of Aircraft*, Vol. 32, No. 4, 1995, pp. 868–874.

[10]Conner, M. D., Tang, D. M., Dowell, E. H., and Virgin, L. N., "Nonlinear Behavior of a Typical Airfoil Section with Control Surface Freeplay: A Numerical and Experimental Study," *Journal of Fluid and Structures*, Vol. 11, No. 1, 1997, pp. 89–109.

[11]"MSC/NASTRAN User's Manual," MacNeal–Schwendler, 1981.

[12]Ueda, T., and Dowell, E. H., "A New Solution Method for Lifting Surfaces in Subsonic Flow," *AIAA Journal*, Vol. 20, No. 3, 1982, pp. 348–355.

[13]Eversman, W., and Pitt, D. M., "Lattice/Doublet Point Method for Lifting Surfaces in Subsonic Flow," *AIAA Journal*, Vol. 28, No. 4, 1991, pp. 572–578.

[14]Roger, K. L., "Airplane Math Modeling Methods for Active Control Design," AGARD Rept. 228, 1977.

[15]Abel, I., "An Analytical Technique for Predicting the Characteristics of a Flexible Wing Equipped with an Active Flutter Suppression System an Comparison with Wind Tunnel Data," NASA TP 1367, 1979.

[16]Karpel, M., and Newman, M., "Accelerated Convergence for Vibration Modes Using the Substructure Coupling Method and Fictitious Coupling Masses," *Israel Journal of Technology*, Vol. 13, Feb. 1975, pp. 55–62.

[17]Karpel, M., "Efficient Vibration Mode Analysis of Aircraft with Multiple External Store Configurations," *Journal of Aircraft*, Vol. 25, No. 8, 1988, pp. 747–751.

[18]Karpel, M., "Design for Active Flutter Suppression and Gust Alleviation Using State-Space Aeroelastic Modeling," *Journal of Aircraft*, Vol. 19, No. 3, 1982, pp. 221–227.

[19]Press, W. H., Flanner, B. P., Teukolsky, S. A., and Vetterling, W. T., *Numerical Recipes: The Art of Scientific Computation*, Cambridge Univ. Press, Cambridge, England, U.K., 1986, pp. 704–716.

[20]Kim, S. H., "Aeroelastic Analysis for Control Surface of Flight Vehicle with Structural Nonlinearities," Ph.D. Dissertation, Korea Advanced Inst. of Science and Technology, Teajeon, Republic of Korea, June 1994.